Mixing gold and iron in nanoparticles by electrical discharges in liquid: A new approach

A.V. Nominé, T. Gries, Cédric Noël, J. Ghanbaja, S. Bruyere, Alexandre Nominé,, V. Milichko, T. Belmonte

Mixing Gold and Iron in nanoparticles by electrical discharges in liquid: a new approach

A.V. Nominé[1], T. Gries[1], C. Noel[1], J. Ghanbaja[1], S. Bruyère[1], A. Nominé[1,2], V. Milichko[1,2], T. Belmonte[1,*]

1. Université de Lorraine, CNRS, IJL, F-54000 Nancy, France
2. ITMO University, St. Petersburg 197101, Russia

* thierry.belmonte@univ-lorraine.fr

Keywords

Discharges in liquids ; Nanoparticles ; non-equilibrium ; immiscible elements ; nanoalloys

Abstract

The possibility to create homogeneous nanoparticles containing iron and gold by nanosecond-pulsed discharges in liquids, without any laser assistance, is demonstrated. Thanks to a new kind of electrode where elements are coated by PVD on a silicon plate, AuFe nanoparticles, ranging from 10 to 50 nm, are synthesized. Depending on their residence time in the discharge, the structure of homogeneous nanoparticles evolves to become a core-shell structure, either nested or not. Larger submicrometric particles (from 100 to 500 nm) are specifically formed with the present process by ejection of liquid droplets from the molten pool created by the discharge on electrode surfaces. These larger particles are produced by solidification of a AuFe shell on a silicon core. This new mechanism can be used to create core-shell particles with a shell containing several, possibly immiscible, elements. Thermal post-treatments performed *in situ* in a TEM microscope show the AuFe shell, where Au and Fe separate, turns either into a Janus structure or into a SiFe core facetted by gold pyramids.

1. introduction

Mixing elements that are thermodynamically immiscible or weakly miscible paves the way to the synthesis of materials with new properties [Zlotea2014, Calvo2015, Glazkova2018, Lerner2016, Oumellal2016, Combettes2020, Nominé2021a, Nominé2021b, Larin2020].

Among the numerous possibilities of binary systems, the Au–Fe system is of great interest from a fundamental point of view due to extended miscibility gaps and deviating crystal structures of its constituents in the bulk, gold being face-centered cubic (fcc) whereas iron is either body-centered cubic (bcc) or fcc. A major advantage of Au-Fe nanostructures is the high magnetic moment of the metallic Fe-rich core compared to its oxide counterparts [Kamp2018]. Keeping the iron metallic may lead to the use of these nanomaterials in numerous applications like electrocatalytic oxygen evolution, magnetic resonance imaging or magnetic thermotherapy [Vassalini2017, Jun2008].

In order to keep the metallic state of the iron core in these AuFe nanoferromagnets, and thus study the properties of these metallic plasmonic structures, many studies resorted to laser ablation in liquid (LAL) to generate different compositions and structures in order to control the final properties of the synthesized objects [Amendola2017, Tymoczko2018]. Among the commonly-encountered structures for Fe and Au formed from liquid droplets, one finds: alloy nanoparticles (NPs) with disordered solid solution (SS) mixture, core-shell (CS) NPs with iron core and gold shell and nested core-shell (NCS) NPs, with one or many cores (**Figs. 1a** to **1d**) [Zelenka2022]. The final internal phase structure (sometimes

named “ultrastructure”) of Au–Fe NPs is strongly affected by the composition and the particle diameter [Magomedov2021, Kamp2018, Kamp2020, Johny2022, Tymoczko2018].

In LAL processes, the prevalence of CS and SS structures is ruled by the target composition and the particle diameter. The formation of CS is favored in iron-rich targets (Fe > 35 mol%), for particles > 10 nm and results in BCC iron crystal structures. Nonequilibrium alloy materials are made of Fe(containing Au)@Au(containing Fe) CS structures where the core and shell are both alloys [Tymoczko2018]. SS NPs would be thermodynamically more stable for diameters < 7 nm, whatever the Fe/Au molar ratio.

Fcc iron-rich phases present in target materials are observed at moderate and Au-rich compositions: $Au_{80}Fe_{20}$ fcc-fcc and $Au_{50}Fe_{50}$ fcc-bcc/fcc [Johny2022]. At Au-low composition: the iron rich-phase is bcc: $Au_{20}Fe_{80}$ fcc-bcc [Johny2022]. The fcc phases at low and high iron content ($Au_{80}Fe_{20}$ and $Au_{20}Fe_{80}$) differ in crystallite size and lattice strain [Johny2022]. However, they merge to single fcc phases at elevated temperatures and form a complex onion-like morphology having a mixed Au-Fe core, a Fe intermediate layer, and a Au-rich shell.

Metastable spherical CS $Au_{20}Fe_{80}$ NPs were transformed by *in situ* heat treatment up to 973 K (700°C) into Janus or cube-shaped Fe-rich core facetted by truncated Au-rich pyramids (**Figs. 1e** and **1f**) depending on the Au/Fe ratio [Kamp2018]. For $Au_{50}Fe_{50}$ NPs, the Au-rich shell is solved into the Fe-rich core, and SS NPs are formed via an intermediate ultrastructure with lamellar segregation.

For crystalline AuFe NPs in the 10 nm range, grown on a hot alumina plate (600°C) [Combettes2020], the shape of the grown NPs is found to strongly evolve with the amount of metal deposited on the Fe core, a transition from a polyhedral Wulff shape of bare iron to a cubic shape taking place as the amount of deposited gold exceeds two monolayers. In this case, Benzo *et al.* [Benzo2019] showed the progressive vanishing of the $\{110\}_{Fe}$ core facets in favor of $\{100\}_{Fe}$ facets with increasing Au deposited thickness.

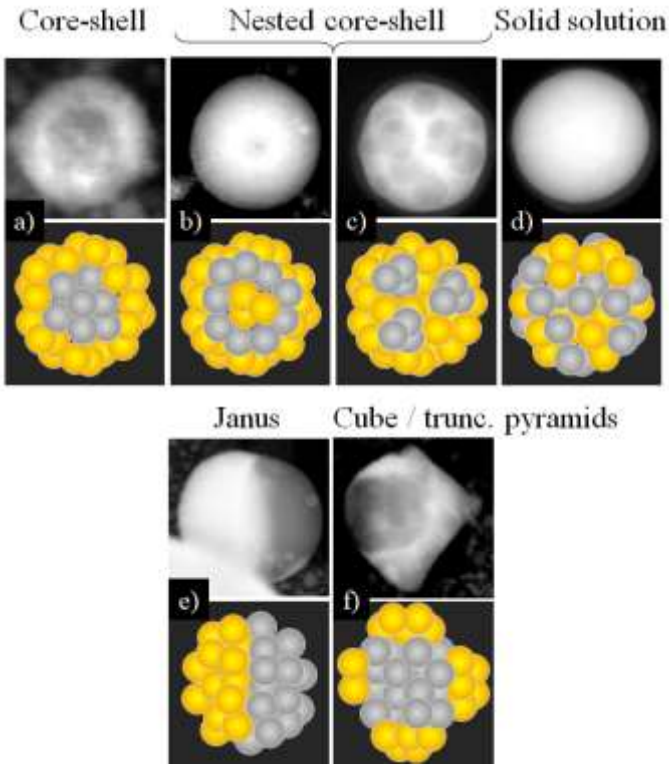

Fig. 1. a) to d): TEM images of commonly-observed nanostructures of AuFe NPs, together with their schematic representations depicted underneath where gold atoms are represented in gold and iron

atoms in grey. a) core-shell (CS) NPs with iron core and gold shell, b) and c) nested core-shell (NCS) NPs, with one or many cores and d) alloy NPs with disordered solid solution mixture. e) and f) nanostructures formed upon *in situ* heating from CS NPs.

In 2018, the possibility to alloy by discharges in liquids Ag and Cu beyond the solubility ranges of one element in the other has been demonstrated by Tarasenka *et al*. [Tarasenka2020] using micro-powders of pure Cu and Ag treated consecutively with two non-equilibrium processes based on plasma and lasers in liquids. More recently, Nag *et al.* [Nag2023] achieved to get similar results using femtosecond laser reduction of solutions containing copper and silver complexes dispersed in a mixture of methanol and isopropyl alcohol.

Nanosecond-pulsed discharges in liquids enable deposition of tens of mJ within nanosecond time scales, which corresponds to huge dissipated power (up to 10 MW and beyond) [Hamdan2014]. These extreme conditions are favorable to the development of large gradients and give access to ultrahigh heating and cooling rates. Thanks to these processes, metastable phases and solid solutions of immiscible elements can be created, with original properties [Nominé2022]. Resorting to liquid nitrogen simply hinders oxidation in the liquid phase.

The possibility of coupling the use of PVD thin films as target-electrodes with discharges in liquids opens up a very large number of possibilities to create new materials from a given set of elements. Thus, it is possible to benefit from the intimate mixing of many elements, even immiscible with each other, in the target-electrode. This enables their simultaneous presence in close vicinity in the discharge and creates conditions that are favorable to the formation of solid solution or desired compounds with given compositions. The second important asset of the present approach is the production of core-shell particles of large dimension with non-miscible elements forming a patterned shell. These two specific designs of particles have never been proposed, to the best of our knowledge, even with laser processes. Sub-micrometric particles are also extremely useful for various application fields. They are easy to collect and few processes provide particles in this range of sizes. They can be used to invent new catalytic properties [Peng2015], new vectors for drug delivery [Tarkistani2021] and new optical properties [Tarasenka2020].

In this work, we investigate to possibility to mix gold and iron and produced nanoalloys directly by discharges in liquid nitrogen, without any laser assistance. In this objective, a new type of electrodes is used, made of a PVD coating deposited on a silicon plate. A special attention is paid to the equilibrium shapes obtained by TEM-*in situ* thermal post-treatment on large particles with silicon cores to better understand their structure.

2. Experimental details

The experimental setup was presented in detail elsewhere [Hamdan2013a]. Briefly, a solid-state switch (Behlke HTS-301-03-GSM), supplied by a high DC voltage power generator (Technix SR15-R-1200–15 kV–80 mA) was connected to a pin-electrode, the other plate electrode being grounded (**Supplemental Material 1**). The voltage rise time was set to 20 ns. Pulses of positive voltage (100 ns in duration) were applied at a frequency of 10 Hz to the power electrode (anode) during 30 minutes. The applied voltage was +5 kV. The two electrodes were immersed in a 100 ml Dewar filled with liquid nitrogen. The inter-electrode gap distance was kept constant during the process (100 µm) by continuous correction with micrometric screws. The W pin electrode was moved along the plate electrode to refresh continuously the surface state of the plate electrode after each discharge (**Fig. S1**, **Supplementary Material**). The pin electrode was made of pure tungsten (99.9 at.%). The plate electrode was made of a gold-iron thin film deposited by magnetron sputtering on a 1 x 1 cm² silicon wafer that was previously cleaned

successively with ultrasonic baths for 10 min in ethanol and 10 min in acetone. The silicon wafer being slightly oxidized, it was covered by a 8 nm-thick amorphous SiO_2 layer (**Fig. 2** and **Fig. S2**, **Supplementary Material**). Gold and iron were co-sputtered during 15 min to form a 675 ± 50 nm-thick layer with a nominal composition of 56 at.% Au and 44 at.% Fe determined by EDX (**Fig. 2**). The power applied to the iron target was 120 W, 40 W to the gold target in a 10 vol.% H_2-90 vol.% Ar atmosphere at 5.8×10^{-3} mbar. At the end of the deposition process, iron sputtering was stopped a bit earlier than gold to deposit a gold layer of about 10 nm during 20 s. This procedure suppressed oxidation of iron in the air before discharge processing in liquid nitrogen. X-ray diffraction showed a pattern that matches the $Fe_{40}Au_{60}$ reference spectrum (JCPDS N° 04-005-6758 [Roberge1973]). The film exhibited a highly-textured structure with a strong dominant (111) orientation (**Fig. S2**, **Supplementary Material**).

Thin films and nanoparticles were characterized by high-resolution transmission electron microscopy (HRTEM) to determine their structure and composition. A JEOL ARM 200F cold FEG TEM/ STEM, equipped with a GIF quantum ER model 965, was operated at 200 kV (point resolution: 0.12 nm). High-angle annular dark-field scanning transmission electron microscopy (HAADF-STEM) and two-dimensional elemental mapping using energy-dispersive X-ray spectroscopy (EDX) were combined to determine the chemical composition of nanoparticles. The DigitalMicrograph® software by Gatan (version 3.30.2016.0) was used to exploit EDX measurements. It can give the average composition of any selected area on the basis of raw EDX data acquired point by point in a map acquisition. For instance, to estimate the average composition of a given spherical nanoparticle, it is sufficient to select a disk over the same section. There are several possible sources of errors on the chemical compositions: the signal level, the detector resolution, calibration factors and the difference between the shape of the object and the selected area. Results provided in this work are deemed to be accurate within a margin of error of about ±2%. Scanning electron microscopy (SEM) observations were carried out using a SEM Quanta 600 FEG by the FEI company. X-ray diffraction measurements were performed with a Bruker D8 ADVANCE diffractometer (Cu-Kα incident radiation, λ = 0.15056 nm) operating in the $\theta/2\theta$ Bragg-Brentano geometry with a step size of 0.02° over a scan range from 20 to 90°.

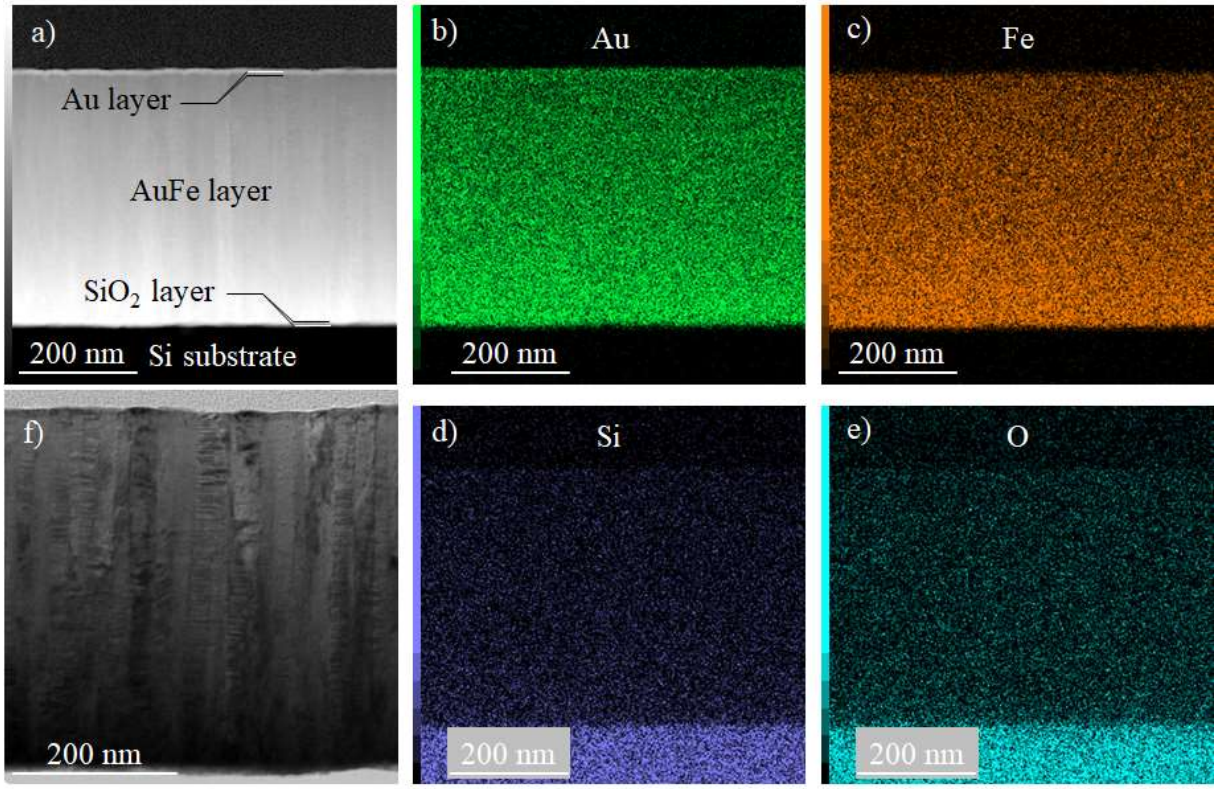

Fig. 2. a) Architecture of the deposited AuFe thin film (HAADF STEM micrograph of the cross-section slice of the film produced by focused-ion beam). The $Au_{56}Fe_{44}$ layer coated by a 10-nm thick gold layer to protect iron from air oxidation. b) to e) Elemental EDX maps of Au (from M_α transition), Fe (K_α), Si (K_α) and O (K_α) showing the distribution of elements within the film. f) TEM bright field image of the film showing its columnar structure.

3. Results and discussion

Nanosecond-pulsed discharges in liquids are known to produce 3 distributions in size [Hamdan2013b]: The largest ones (>100 nm in diameter) are created by emission of droplets from the liquid pool formed when the discharge hits the electrode surface. They are submitted to high stress levels by fast thermal quenching. Nanoparticles with diameters distributed around 10 to 20 nm have structure defects and are synthesized in the discharge and post-discharge for longer residence time than the smallest NPs. These latter (<5 nm) are synthesized in the plasma and will not be studied in this work.

Overview images of particles produced in this work are given in **Fig. S3** (Supplementary Material) together with size distributions. Reproducibility of results from one set of experiments to another for selected conditions was checked and found very satisfactory.

The production of nanoparticles (from 10 to 50 nm typically) is characterized by the presence of Au and Fe, sometimes weakly oxidized, with possible traces of Si and W limited to a few atomic percent (**Fig. 3**). Of course, other nanoparticles, for instance made of Si or W, are also found. Thereafter, AuFe nanoparticles will be treated without taking into account Si and W. In the presented example, the Au/Fe ratio is significantly lower than its value in the PVD thin film (it decreases from ~1.3 to ~0.7). One reason why nanoparticles have compositions that can drift could be the difference of 473 K in melting temperatures between gold and iron, leading to differential evaporation when the particle is

already formed and transits in a hot region. This could be also due to the way Au and Fe vapours condensate in given conditions, forming particles.

All compositions given hereinafter refer to compositions of the selected particles, averaged over their volume, and only to these particles.

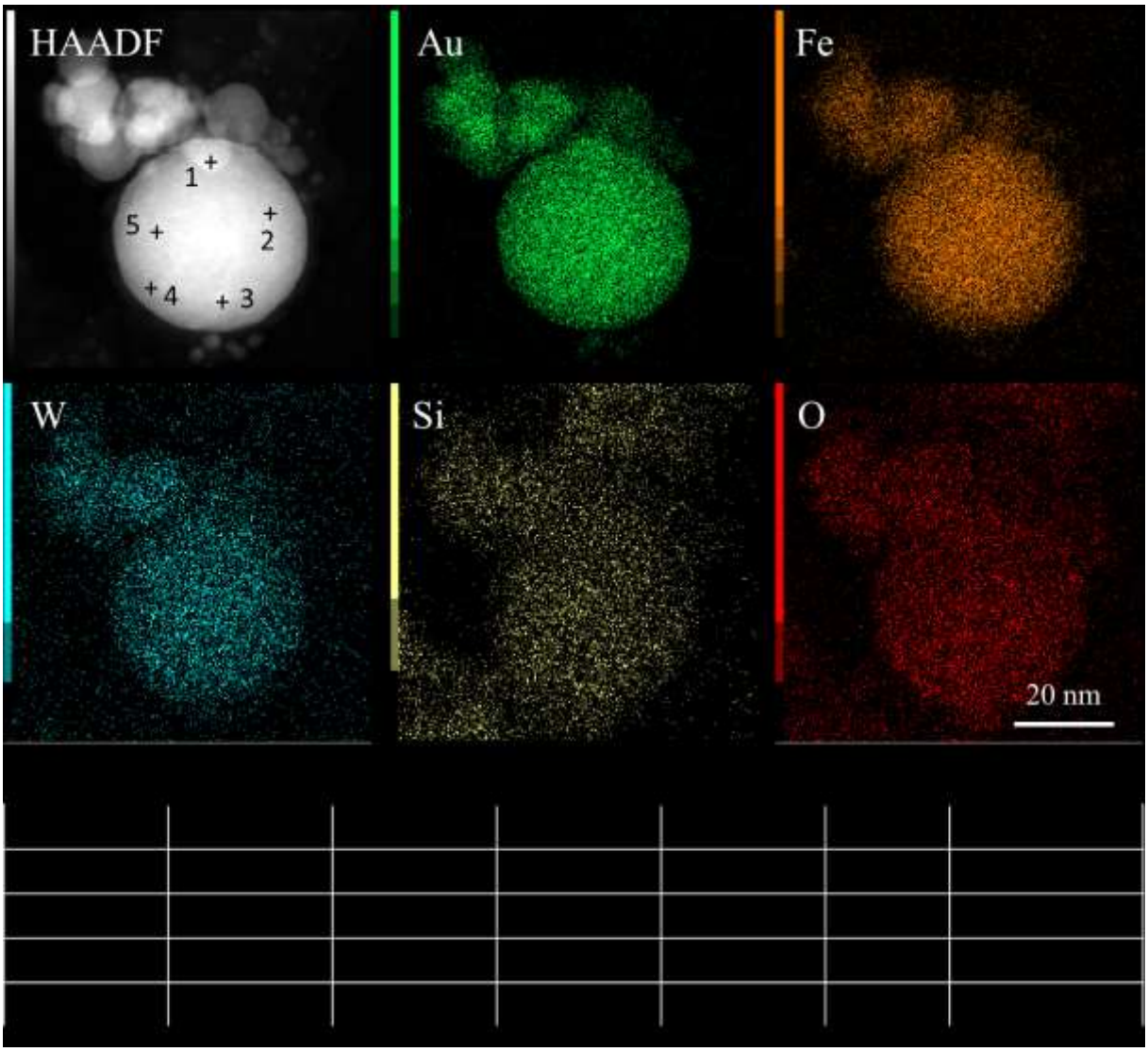

Fig. 3. Overview of nanoparticles produced by nanosecond-pulsed discharges in liquid nitrogen. High-angle annular dark field image of a set of nanoparticles. STEM-EDX elemental maps of Au (from M_α transition), Fe (K_α), W (L_α), Si (K_α) and O (K_α). In this example, nanoparticles are weakly oxidized and made of Au, Fe and traces of W and Si. Localized EDX measurements performed on 5 different spots are materialized by crosses in the HAADF image. Corresponding compositions are given in the table in at.%. We recall here that the nominal composition of the PVD thin film is 56%Au-44%Fe.

In **Fig. 4**, three different structures of AuFe nanoparticles with similar sizes (30-40 nm) and compositions (from 49 to 57 at.% in gold balanced by iron) are depicted: core-shell, segregated and homogeneous. We assume here that particles are spherical and have compositions that vary only along the radius. These two assumptions are not strictly valid, considering images and profiles given in Fig. 4, but they are acceptable in first order.

What is meant by “homogeneous” here is the fact that segregation is too small to be resolved (typically lower than 2-3 nm). In the kind of objects, gold and iron are usually described as forming a solid solution, both atoms coexisting in a close vicinity without forming apparent domains.

It is often considered as a nanoalloy as diffraction patterns verify Vegard’s law. In this case, lattice parameters are assumed to vary linearly with the composition from one pure structure to the other. So, for a given solid solution, it possible to deduce from its lattice parameters the composition it adopts, as discussed hereafter.

On the contrary, in segregated structures, Au and Fe nanodomains of 5-10 nm in size can be distinguished easily, especially with line profiles that are supplied with the elemental maps and where multiple local extrema are found. In core-shell structures, all nanoparticles synthesized in this work are characterized by a core rich in iron surrounded by a shell rich in gold. Indeed, the shape of elemental profiles presented in this work match with those provided by other authors [Tymoczko2018, Kamp2020]. To know the precise composition of each zone, Abel transform of raw profiles is needed. However, applying the transformation to the present data lacks accuracy because it is too noisy and not perfectly symmetrical.

This kind of particle is characterized by a distribution of gold with two local maxima on each edge of the diameter chosen as measure line. In the gold-rich shell, the beam crosses the particle without crossing the core and the recorded signal is directly informative on the shell composition. As gold is mainly present, the shell appears whiter on HAADF images.

For nested core-shell structures, gold is present as a set of small particles (from 3 to 5 nm typically) embedded in a gold matrix. Maxima of intensity in the iron profile appear each time the beam crosses a small particle, which corresponds to minima of intensity in the gold profile. Theses extrema are not only located at the particle edges, like in core-shell structures, but anywhere in the particle depending on the presence of iron inclusions along a given line profile.

Homogeneous Au-Fe nanoparticles are well crystallized but often highly faulted (**Fig. 5**). Au-Fe nanoparticles are more or less oxidized and the presence of twin defects (**Figs. 5b and d**) is likely due to the development of stress, either when the particle is quenched or when it is oxidized.

They have *d*-spacing values of 0.226 nm, 0.143 and 0.114 (**Fig. 5a**) deduced both from FFT analyses and diffraction patterns, close to the (111), (220) and (200)-$Fe_{40}Au_{60}$ which gives ratios of Fe to Au varying from 25 to 33% (**Fig. 5h**), *i.e.* compositions consistent with STEM-EDX data, assuming the validity of Vegard's law introduced previously. The corresponding range of compositions from 25 to 33% of solid solution nanoparticles is reported in the macroscopic Au-Fe phase diagram together with the nominal composition of the electrode material (**Fig. 5g**), to illustrate the drift in composition due to discharge processing.

High-resolution images (**Figs. e and f**) of areas chosen in the two well-crystallized particles showed in **Fig. 5c** confirm that the lattice interspacing are close to 0.266 nm, in agreement with data given by FFT analyses and diffraction patterns.

It is important to notice that for some particles, the Au/Fe ratio reaches the nominal composition of the PVD thin film, which means that the drift of the composition mentioned earlier is not systematic and likely due to thermal treatments within the discharge.

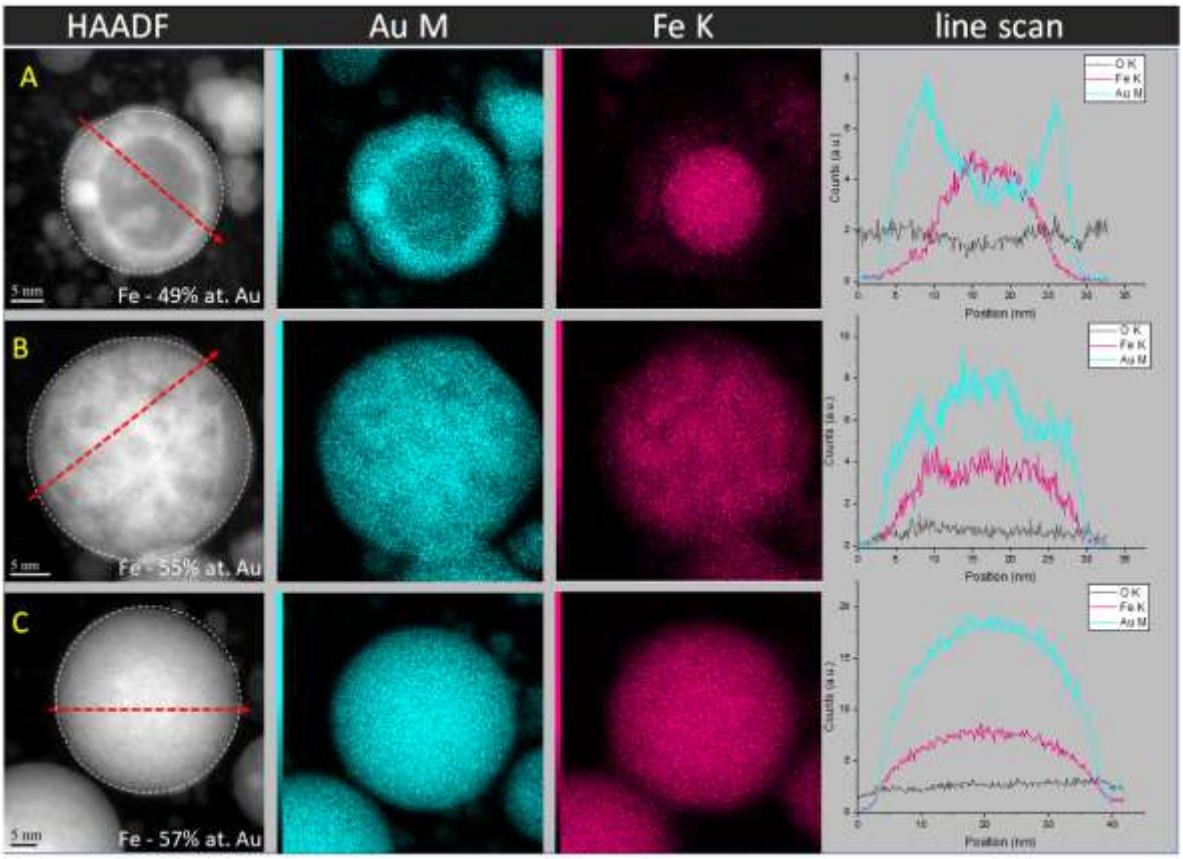

Average concentration [at.%]	NP A	NP B	NP C
O K	44.0	12.5	19.3
Fe K	28.5	39.0	34.4
Au M	27.5	48.5	46.3
Total	100	100	100
Fe K	51.0	44.6	42.6
Au M	49.0	55.4	57.4
Total	100	100	100

Fig. 4. Examples of the three types of small AuFe nanoparticles synthesised by nanosecond-pulsed discharges in liquid nitrogen with similar sizes and Fe/Au ratios: core-shell, segregated and homogeneous. High-angle annular dark-field images. STEM-EDX elemental maps of gold (from M_α transition) and iron (K_α) and their distribution profiles along the red dotted lines. Average compositions (with and without oxygen) are given for each particle in the table. They are determined from areas showed by dotted circles in HAADF images.

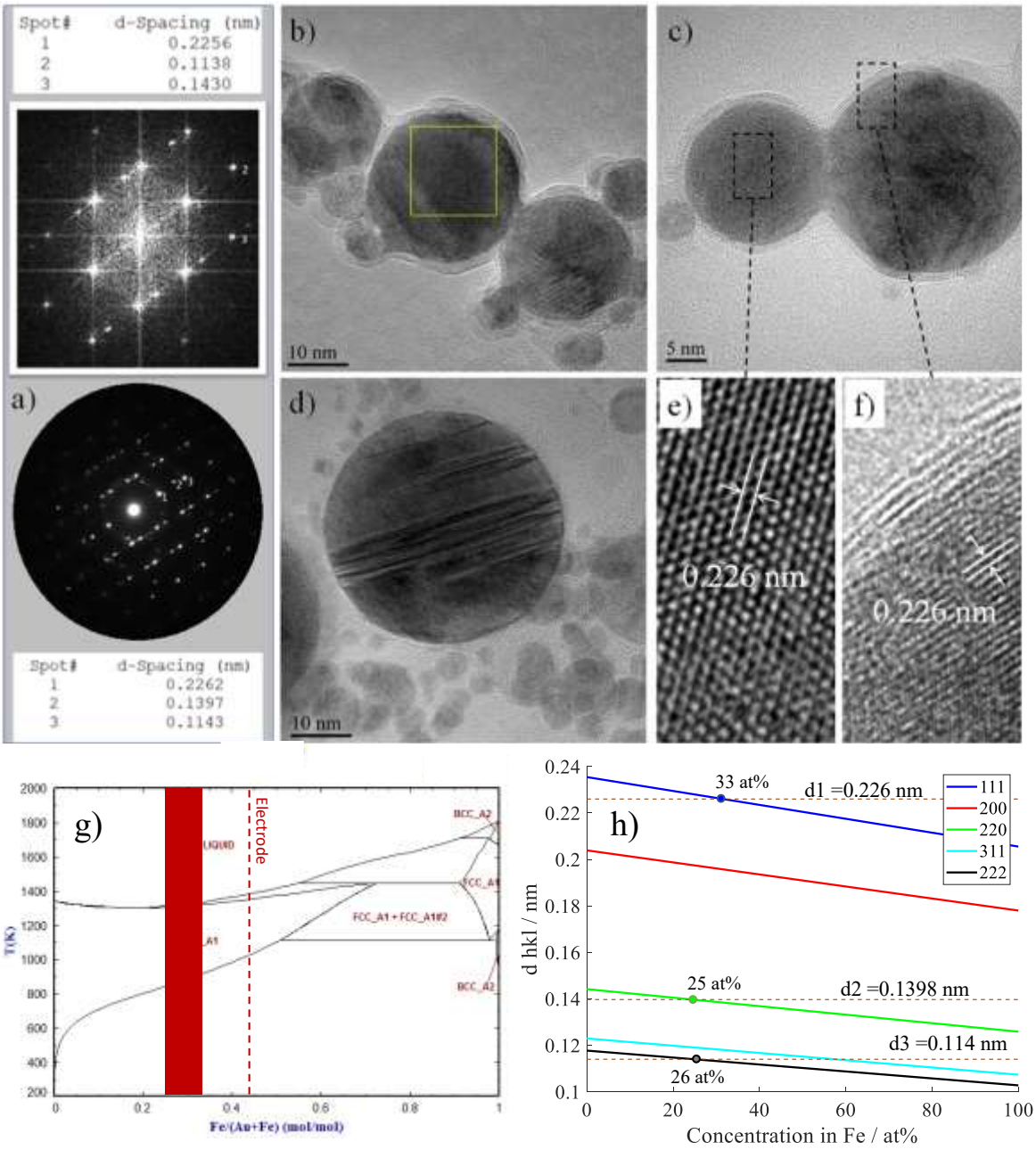

Fig. 5. a) Fast-Fourier transform (top) of the yellow-framed area in the TEM-image shown in b) and diffraction pattern (bottom) made of the same region. 3 spots were selected in the FFT image to determine the d-values given in the insert b) Example of slightly-oxidized AuFe nanoparticles with twin defects c) Another example of AuFe nanoparticles with d-spacing showed in e) and f) that matches with the $Fe_{40}Au_{60}$ structure identified in the PVD film d) Example of a highly faulted AuFe nanoparticles with twin defects e) and f) High-resolution images of the areas in dotted frames showing the well-crystallized structure of the nanoparticles and the surface oxide layer. g) Au-Fe phase diagram locating the composition of the AuFe homogeneous nanoparticles and the composition of the PVD thin film. h) Estimates of the iron concentration in the iron content in the AuFe homogeneous nanoparticle from Vegard's law.

The process produces also large submicrometric particles with diameters ranging from 100 nm to < 1 µm typically that are either containing silicon with possibly iron and gold or made of tungsten (**Fig. 6** and **Fig. S4**, **Supplementary Material**). The presence of silicon is due to discharges that erode the

substrate deeper that the thickness of AuFe thin films. This can be due to high-energy discharges (typically, the liquid well formed by a single impact is several hundreds of nanometres deep [Hamdan2013a]) or to multiple discharge events on the same spot. The presence of silicon is the footprint of these large particles whose formation is due to ejection of droplets from the liquid well formed by the discharge during the erosion of the electrode [Hamdan2013a]. Similarly, the synthesis of W particles from the pin electrode proceeds alike and leads to production of large W particles, the refractory behaviour of W (its melting point is 3695 K vs 1811 K for Fe, 1683 for Si and 1338 K for Au) making the welding of the electrode harder and the occurrence of large W particles lower. All large objects are more or less oxidized, often at their surface, and exhibit different compositions depending on their formation and trajectory within the discharge.

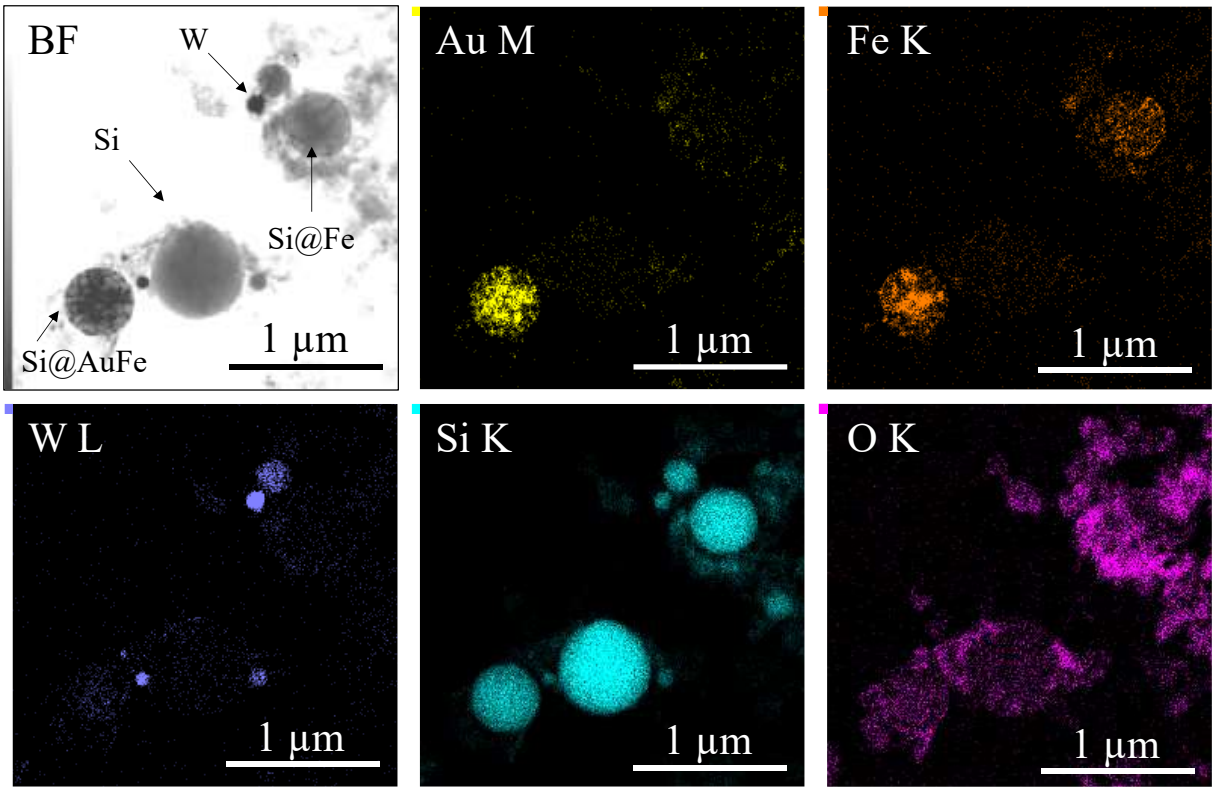

Fig. 6. Overview of particles produced by nanosecond-pulsed discharges in liquid nitrogen. Bright field STEM image. TEM-EDX elemental maps of Au (from M_α transition), Fe (K_α), W (L_α), Si (K_α) and O (K_α). In this example, the largest (submicrometric, *i.e.* > 100 nm in diameter) particles (depicted by arrows) are Si@AuFe, Si, Si@Fe and W (**Fig. S4**, **Supplementary Material**).

The most interesting feature of Si@AuFe large particles is that Au and Fe are usually present on the outermost part of the particle, as if the structure was formed by crystallization of Au and Fe separated islands floating on a silicon droplet (**Fig. S5**, **Supplementary Material**). Iron, present in the shell around the particle core, gets slightly oxidized once in the air. To check this assumption, *in situ* heat treatments under the high vacuum (~2×10^{-5} Pa) of the TEM were performed to observe how structures evolve.

As temperature rises from 873 to 1173 K (**Fig. 7**), gold and iron islands forming separate networks, present before heating, coarsen and form larger domains, still separate. As both elements regroup, parts of the surface get uncovered, likely because the shell is initially too thin, revealing the silicon core underneath.

As temperature rises, iron and gold form segregated islands that are larger and larger. The overall composition of the particle hardly varies before and after heating as showed by elemental compositions given in **Fig. 7**. Fluctuation of compositions are likely due the change of the shape of the particle, which is not perfectly round-shaped after heating.

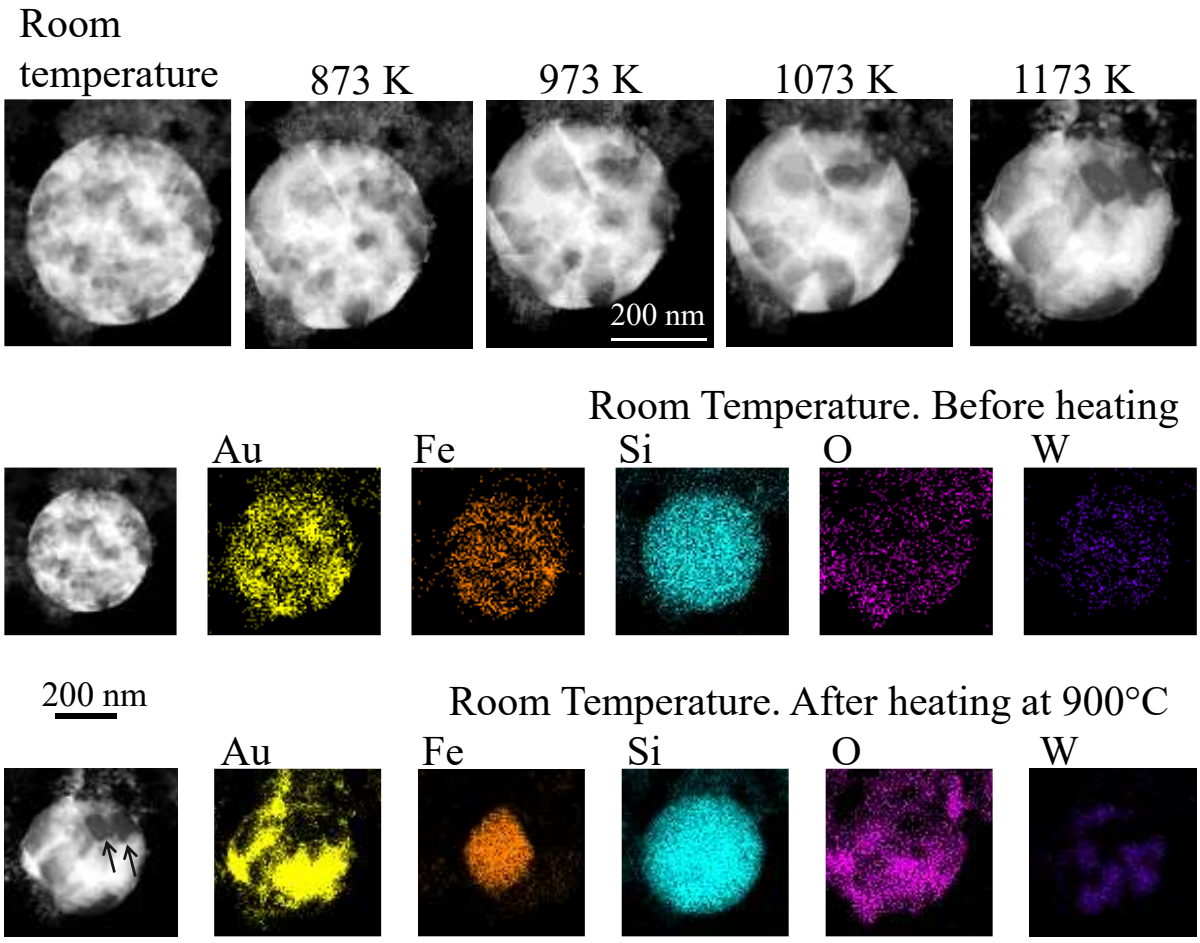

Average concentration [at.%]	Au L	Fe K	Si K	O K	W L	Total
NP before heating	6.9	7.9	79.8	2.6	2.8	100
NP after heating	7.9	10.3	77.3	1.6	2.9	100

Fig. 7. *In situ* heat treatment of a Si@AuFe particle, weakly oxidized (Si: 79, Fe: 10, Au: 10, O: 0.5, W: 0.5 at.%). Top: HAADF STEM images of the particle. Middle and bottom: HAADF STEM image and elemental maps of the nanoparticles before and after heating. Arrows in HAADF image (bottom line) indicate two areas uncovered by Au and W and revealing the silicon core. Gold and iron islands forming separate networks, present before heating, coarsen and form larger separate domains. Average compositions of particles are given before and after heating.

Other Si@AuFe particles, showed by two vertical arrows in **Fig. S6**, **Supplementary Material** and individually in **Fig. 8**, evolve structurally in a slightly different way. Their structure starts changing well below the melting temperatures of pure elements, which is not the case of the silicon particles, showed

by a horizontal arrow in **Fig. S6**, **Supplementary Material** and showed all together in **Fig. 8**. This evolution of the structure of Si@AuFe particles is then only due to thermodynamic segregations.

In the larger Si@AuFe particle, iron and gold fully separate and form a Janus shell on a silicon core (another similar example is given in **Fig. S7**, **Supplementary Material**). Fe and Au separation is predicted by the Langmuir-McLean mechanism for binary mixtures [McLean1957]. In the smaller Si@AuFe particle, gold and iron move outwards, segregating at the free surface of a silicon core enriched in Fe and probably forming a SiFe alloy. In this case, the shape of the silicon given by the EDX map is no longer spherical but it exhibits after heating facets (see also **Fig. S7**, **Supplementary Material**) connected to Au pyramids. As showed in **Fig. 8**, if silicon does not move when it is iron-free, the presence of iron may contribute to its alloying. At 1173 K, several SiFe alloys are available, depending on the atomic composition, namely three solid solutions: α-$Fe_{100-x}Si_{x=0-13}$, α_2-$Fe_{100-x}Si_{x=13-16}$ and α_1-$Fe_{100-x}Si_{x=16-28}$, and three compounds: η-Fe_5Si_3 (hexagonal), ε-FeSi (cubic) and ζ_β-$FeSi_2$ (orthorhombic). It is also true with tungsten that forms WSi_2 (tetragonal) or W_5Si_3 (tetragonal) with silicon. More details are provided as **Fig. S8**, **Supplementary Material**.

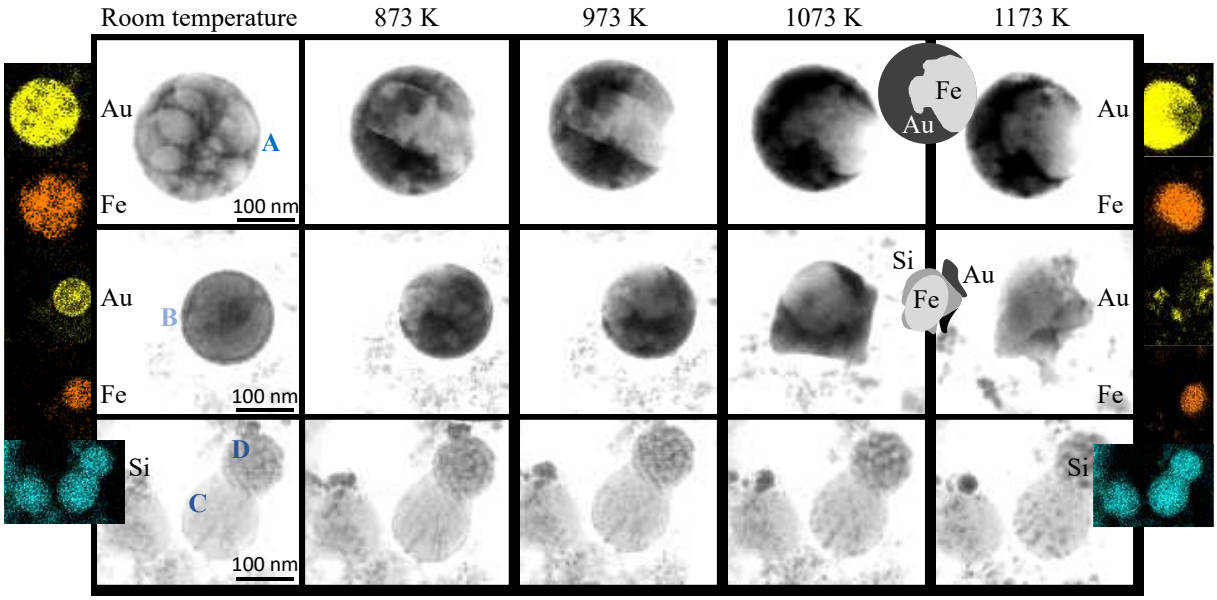

Particle	NP A		NP B		NP C		NP D	
Element Conentration, [at.%]	before	after	before	after	before	after	before	after
Si K	57.9	55.4	54.7	62.4	91.8	93.3	81.3	84.6
Fe K	18.4	21.8	20.5	22.2	0.3	0.1	0.6	0.2
Au L	15.7	16.9	13.3	3.5	0.4	0.3	0	1.0
O K	4.9	2.3	3.7	0.7	6.7	4.6	9.1	6.4
W L	3.1	3.6	7.8	11.2	0.8	1.7	9.0	7.8
Total	100	100	100	100	100	100	100	100

Fig. 8. Examples of two Si@AuFe particles (bright field STEM images, top – 225 nm in diameter ; before heating Si: 63, Fe: 21, Au: 15, O: 0.5, W: 0.5 at.% – and middle – 160 nm ; before heating Si: 56, Fe: 25, Au: 13.5, O: 0.5, W: 5 at.% –) heated from room temperature to 1173 K (900°C). Bottom: three silicon particles (145, 150 and 180 nm in diameter ; after heating Si: 95.5, Fe: 0.5, Au: 1, O: 2.5, W: 0.5 at.%), submitted to the same heat treatment. The Au, Fe and Si elemental maps are also provided for the

initial and final states. A schematic of the final shape of the two Si@AuFe particles at 900°C is added on the left-hand side of the right column. For the middle one, at 1073, the SiFe core facetted by gold pyramids is clearly visible. Silicon distribution in the AuFe particle at the top overlaps those of Au and Fe. Average compositions are given before and after heating. Complementary information is given in **Fig. S7**, **Supplementary Material**.

Two situations occur depending on whether the discharge erodes fully or not the PVD layer (**Fig. 9**). In the former case, a part of the silicon substrate is etched and leaves the surface together with gold and silicon. In the latter, only gold and iron are emitted.

When AuFe NPs are synthesized, free of silicon, they can experience different trajectories, leading to variable heating durations. If they are small in size, their composition can be frozen if their residence time is short. Indeed, quenching rates in these processes are known to be very high (about 10^{10} to 10^{12} K s^{-1}) [Nominé2021b]. This condition is mandatory to get homogeneous NPs as those showed in **Fig. 4**. However, the possibility to produce this kind of nanoalloys here is clearly associated with the possibility of starting from an intimate mixing of Au and Fe in the electrode. Resorting to PVD layers, as we did it here, offers the capability of producing non-equilibrium coating, which is the major asset of this deposition process. As both metals are eroded together, their vapours remain close in the discharge, which favours their simultaneous condensation into homogeneous NPs. Thanks to this electrode design, no laser post-treatment is needed, making the present process very promising for the production of new nanoalloys. When NPs stay longer in high-temperature areas of the discharge, elements segregate and form nested core-shell NP that can evolve for even longer time to form core-shell NP (**Fig. 9a**).

Small nanoparticles are very similar in shape and size to those produced by laser ablation in liquids [Amendola2017, Kamp2018]. Both types of processes can create spherical solid solution, core-shell and nested core-shell AuFe particles. For large particles, no example of processes leading to similar nano-objects seems to be available.

Large particles are most often ejected as droplets from the molten pool formed at the electrode surface when hit by the discharge. Because of the very specific structure of Si@AuFe large particles, the following growth mechanism is proposed (**Fig. 9b**):

- Step 1: a part of the substrate coated by the PVD AuFe layer is ejected when hit by the discharge.
- Step 2: The particle in the discharge is heated and Au and Fe get redistributed over the surface without mixing.
- Step 3: Particles can be more or less oxidized in the air when they are taken out of the liquid, depending on the period of time they spend before analysis,
- Step 4: the AuFe shell is restructured under heating in the TEM, revealing locally the silicon core.

As far as we know, this mechanism is the first of the kind described to date and it is associated here again with the use of PVD thin films as surface material of electrode. As AuFe and Si are eroded as a stack, the final configuration of Si@AuFe particles conserves the initial spatial distribution of the elements. The reason why gold or iron do not form any alloy with silicon at this stage is either due to the presence of the silica layer at the interface between the PVD coating and the substrate (**Fig.1**), which limits interdiffusion between elements or, more likely, to the short time during which interdiffusion is possible before the particle is cold enough to stop atomic transport. This mechanism

could be advantageously used to create Janus particles with new surface properties as the composition of the shell can be as complex as wished.

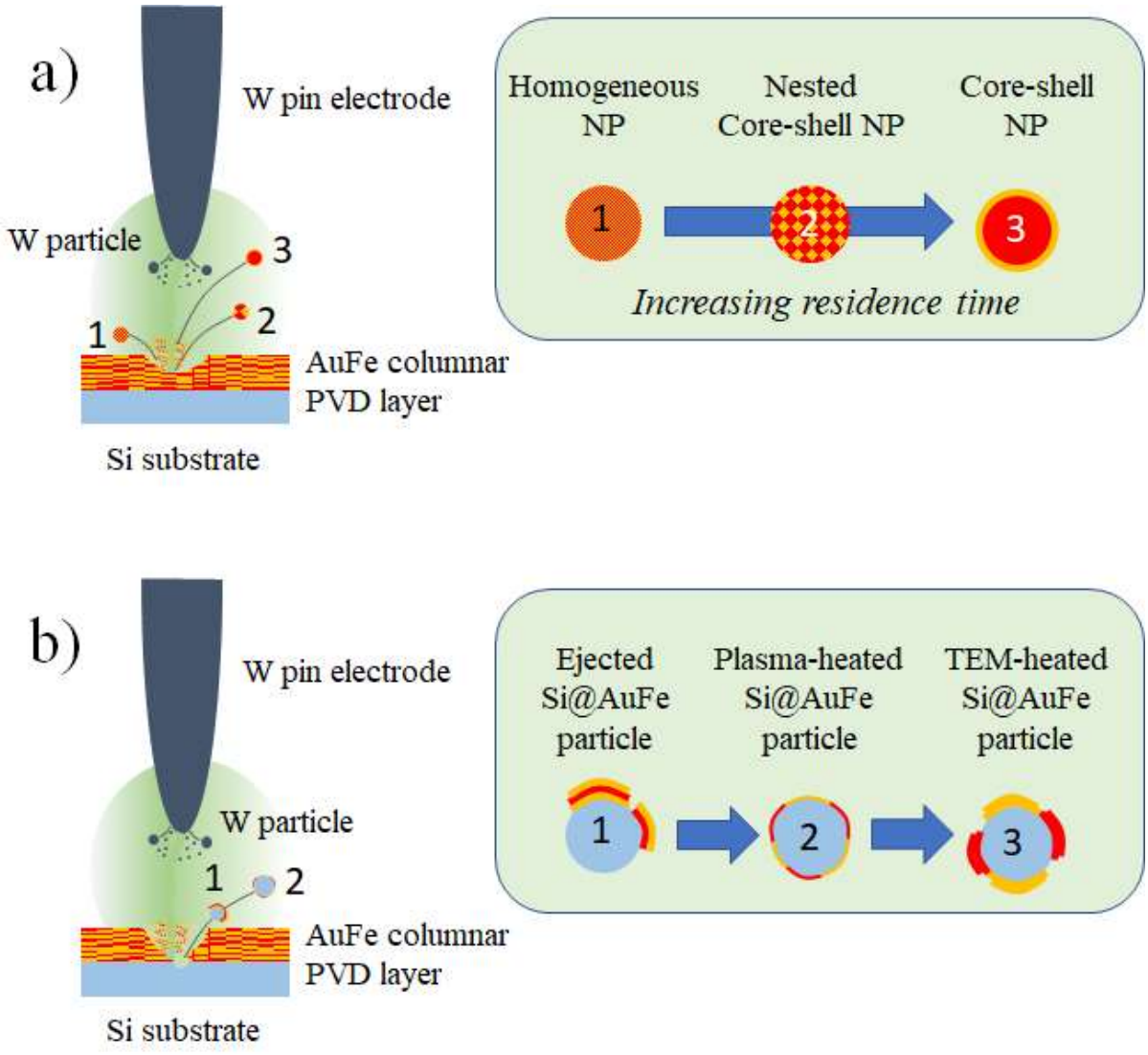

Fig. 9. Possible mechanisms for the formation of AuFe NPs and Si@AuFe large particles. a) If the PVD coating is not fully etched, AuFe NPs are synthesized and adopt different structures in the discharge: homogeneous, nested core-shell or core-shell from short to long residence time. b) If the PVD coating is fully etched, large particles made of silicon and containing variable amounts of gold and iron are ejected from the impact area.

4. Conclusion and perspective

The present process used for the synthesis of AuFe nanoparticles, based on nanosecond-pulsed electrical discharges in liquid nitrogen, is the first of the kind enabling the formation of homogeneous AuFe nanoparticles without resorting to any laser treatment. It is attributed to the intimate premixing of the two elements deposited by PVD sputtering. Core-shell and nested core-shell NPs are also produced. The use of PVD coatings as electrodes gives access to a much broader panel of materials than those available with electrodes made of raw materials.

When the silicon wafer is etched, Si@AuFe large particles (> 100 nm) are synthesized and show a specific structure with iron and gold forming islands. It is produced by a new mechanism where Au and Fe coat a part of the silicon core and are redistributed next by a heat treatment within the discharge to form a continuous shell. Then, it seems very likely to achieve a reduction in size of these particles by using thinner PVD coatings and lower energy in discharges, enabling new designs of nanoalloys.

Unique ultrastructures with the Au shell protecting the magnetic core against oxidation is highly interesting for the long-term stability of the magnetic composites and they might be used for application in areas such as radiation shielding or transparent-conductive coatings [Kamp2020]. Large particles with silicon cores and Au-Fe patterned shells should exhibit original non-linear optical properties like Si@Au hybrids created by laser ablation and that generate white light for ultrabroadband nanospectroscopy [Makarov2018].

The control of the movement of the pin electrode facing the PVD-coated plate electrode is essential to provide a better control of the process. As the charge dissipated per discharge controls the depth of the liquid well at impact, it must be delivered accurately and at renewed position on an always-fresh surface. The capability of this process to mix non-miscible elements straightforwardly and to form core-shell structures by eroding the substrate together with the PVD coating offers interesting ways to mastering the design of complex NPs.

CRediT authorship contribution statement

Anna V. Nominé: Investigation, Methodology. **Thomas Gries**: Investigation, Methodology. **Cédric Noël**: Investigation, Methodology. **Jaafar Ghanbaja**: Data curation; Formal analysis. **Stéphanie Bruyère**: Data curation; Formal analysis. **Alexandre Nominé**: Methodology, Data curation. **Valentin Milichko**: Supervision. **Thierry Belmonte**: Supervision, Writing - original draft.

Declaration of competing interest

The authors declare that they have no known competing financial interests or personal relationships that could have appeared to influence the work reported in this paper.

Data availability

Data will be made available on request.

Acknowledgments

The authors acknowledge the French PIA (programme d'investissements d'avenir) project Lorraine Université d'Excellence (Ref. ANR-15-IDEX-04-LUE) for financial support.

REFERENCES

[Amendola2017] V. Amendola, S. Scaramuzza, F. Carraro, E. Cattaruzza, Formation of alloy nanoparticles by laser ablation of Au/Fe multilayer films in liquid environment, J. Colloid Interface Sci. 489 (2017) 18–27.

[Benzo2019] P. Benzo, S. Combettes, B. Pécassou, N. Combe, M. Benoit, M. Respaud, M. J. Casanove, Role of the shell thickness in the core transformation of magnetic core (Fe)-shell (Au) nanoparticles, Phys. Rev. Mater. 3 (2019) 096001.

[Calvo2015] F. Calvo, Thermodynamics of nanoalloys, Phys. Chem. Chem. Phys. 17 (2015) 27922–27939.

[Combettes2020] S. Combettes, J. Lam, P. Benzo, A. Ponchet, M. J. Casanove, F. Calvo , M. Benoit, How interface properties control the equilibrium shape of core–shell Fe–Au and Fe–Ag nanoparticles, Nanoscale 12 (2020) 18079–18090.

[Glazkova2018] E. A. Glazkova, O.V. Bakina, M.I. Lerner, A.V. Pervikov, Synthesis and applications of bimetallic nanoparticles of immiscible elements, Recent. Pat. Nanotechnol. 12 (2018) 132–142.

[Hamdan2013a] A. Hamdan, C. Noel, F. Kosior, G. Henrion, T. Belmonte, Impacts created on various materials by micro-discharges in heptane: Influence of the dissipated charge, J. Appl. Phys. 113 (2013) 043301.

[Hamdan2013b] A. Hamdan, C. Noel, J. Ghanbaja, S. Migot-Choux, T. Belmonte, Synthesis of platinum embedded in amorphous carbon by micro-gap discharge in heptane, Mater. Chem. Phys. 142 (2013) 199–206.

[Hamdan2014] A. Hamdan, C. Noël, J. Ghanbaja, T. Belmonte, Comparison of aluminium nanostructures created by discharges in various dielectric liquids, Plasma Chem. Plasma Process. 34 (2014) 1101–1114.

[Johny2022] J. Johny, O. Prymak, M. Kamp, F. Calvo, S. H. Kim, A. Tymoczko, A. El-Zoka, C. Rehbock, U. Schürmann, B. Gault, L. Kienle, S. Barcikowski, Multidimensional thermally-induced transformation of nest-structured complex Au-Fe nanoalloys towards equilibrium, Nano Res. 15 (2022) 581–592.

[Jun2008] Y. W. Jun, J. H. Lee, J. Cheon, Chemical design of nanoparticle probes for high-performance magnetic resonance imaging, Angew. Chem. Int. Ed. 47 (2008) 5122–5135.

[Kamp2018] M. Kamp, A. Tymoczko, U. Schürmann, J. Jakobi, C. Rehbock, K. Rätzke, S. Barcikowski, L. Kienle, Temperature-dependent ultrastructure transformation of Au–Fe nanoparticles investigated by in situ scanning transmission electron microscopy, Cryst. Growth Des. 18 (2018) 5434–5440.

[Kamp2020] M. Kamp, A. Tymoczko, R. Popescu, U. Schürmann, R. Nadarajah, B. Gökce, C. Rehbock, D. Gerthsen, S. Barcikowski, L. Kienle, Composition and structure of magnetic high-temperature-phase, stable Fe–Au core–shell nanoparticles with zero-valent bcc Fe core, Nanoscale Adv. 2 (2020) 3912–3920.

[Larin2020] A. O. Larin, A. Nominé, E. I. Ageev, J. Ghanbaja, L.N. Kolotova, S. V. Starikov, S. Bruyère, T. Belmonte, S. V. Makarov, D. A. Zuev, Plasmonic nanosponges filled with silicon for enhanced white light emission, Nanoscale 12 (2020) 1013–1021.

[Lerner2016] M. I. Lerner, A. V. Pervikov, E. A. Glazkova, N. V. Svarovskaya, A. S. Lozhkomoev, S. G. Psakhie, Structures of binary metallic nanoparticles produced by electrical explosion of two wires from immiscible elements, Powder Technol. 288 (2016) 371–378.

[McLean1957] D. McLean, Grain boundaries in metals. Clarendon Press Oxford, (1957) 346 pages. See also S. Hofmann, Segregation to surfaces and interfaces, Scan. Electron. Microscopy 1985 (3) (1985) 16.

[Magomedov2021] M. N. Magomedov, Changes in the structure of the Au–Fe alloy with a change in the concentration and with a decrease of the nanocrystal size, Solid State Sci. 120, (2021) 106721.

[Makarov2018] S. V. Makarov, I. S. Sinev, V. A. Milichko, F. E. Komissarenko, D. A. Zuev, E. V. Ushakova, I.S. Mukhin, Y.F. Yu, A.I. Kuznetsov, P.A. Belov, I.V. Iorsh, A.N. Poddubny, A.K. Samusev, Y. S. Kivshar, Nanoscale generation of white light for ultrabroadband nanospectroscopy, Nano Lett. 18 (2018) 535–539.

[Nag2023] A. Nag, C. M. Nguyen, K. M. Tibbetts, Heterogeneous to homogeneous Cu–Ag nanoparticles by laser reduction in liquid, Appl. Surf. Sci. 610 (2023) 155384.

[Nominé2021a] A. V. Nominé, T. Gries, C. Noel, A. Nominé, V. Milichko, T. Belmonte, Synthesis of nanomaterials by electrode erosion using discharges in liquids, J. Appl. Phys. 130 (2021) 151101.

[Nominé2021b] A. V. Nominé, N. Tarasenka, A. Nevar, M. Nedel'Ko, H. Kabbara, A. Nomine, S. Bruyère, J. Ghanbaja, C. Noel, A. Krasilin, G. Zograf, V. Milichko, N. Kulachenkov, S. Makarov, N. Tarasenko, T. Belmonte, Alloying nanoparticles by discharges in liquids: a quest for metastability, Plasma Phys. Control. Fusion 64 (2021) 014003.

[Nominé2022] A. V. Nominé, N. Tarasenka, A. Nevar, M. Nedel'Ko, H. Kabbara, A. Nomine, S Bruyère, J Ghanbaja, C Noel, A Krasilin, G Zograf, V Milichko, N Kulachenkov, S Makarov, N Tarasenko, T. Belmonte, Alloying nanoparticles by discharges in liquids: a quest for metastability. Plasma Phys. Control. Fusion 64 (2021) 014003.

[Oumellal2016] Y. Oumellal, J. M. Joubert, C. M. Ghimbeu, J. M. Le Meins, J. Bourgon, C. Zlotea, Synthesis and stability of Pd–Rh nanoalloys with fully tunable particle size and composition, Nano-Struct. Nano-Objects 7 (2016) 92–100.

[Peng2015] H. Peng, N. G. Akhmedov, Y. F. Liang, N. Jiao, X. Shi, Synergistic gold and iron dual catalysis: Preferred radical addition toward vinyl–gold intermediate over alkene, J. Am. Chem. Soc. 137 (2015) 8912–8915.

[Reguera2017] J. Reguera, D. J. de Aberasturi, M. Henriksen-Lacey, J. Langer, A. Espinosa, B. Szczupak, C. Wilhelm, L. M. Liz-Marzán, Janus plasmonic–magnetic gold–iron oxide nanoparticles as contrast agents for multimodal imaging, Nanoscale 9 (2017) 9467–9480.

[Roberge1973] R. Roberge, G. M. Leak, A study of iron in gold–iron alloys, Phys. Status Solidi A 19 (1973) 695–705.

[Tarasenka2020] N. Tarasenka, A. Nominé, A. Nevar, M. Nedelko, H. Kabbara, S. Bruyère, J. Ghanbaja, C. Noel, A. Krasilin, G. Zograf, V. Milichko, N. Kulachenkov, S. Makarov, T. Belmonte, N. Tarasenko, Synergistic effect of plasma and laser processes in liquid for alloyed-nanoparticle synthesis, Phys. Rev. Appl. 13 (2020) 014021.

[Tarkistani2021] M. A. M. Tarkistani, V. Komalla, V. Kayser, Recent advances in the use of iron–gold hybrid nanoparticles for biomedical applications, Nanomater. 11 (2021) 1227.

[Tymoczko2018] A. Tymoczko, M. Kamp, O. Prymak, C. Rehbock, J. Jakobi, U. Schürmann, L. Kienle, S. Barcikowski, How the crystal structure and phase segregation of Au–Fe alloy nanoparticles are ruled by the molar fraction and size, Nanoscale 10 (2018) 16434–16437.

[Vassalini2017] I. Vassalini, L. Borgese, S. Mariz, M. Polizzi, G. Aquilanti, P. Ghigna, A. Sartorel, V. Amendola, I. Alessandri, Enhanced Electrocatalytic Oxygen Evolution in Au–Fe Nanoalloys, Angew. Chem. Int. Ed. 56 (2017) 6589–6593.

[Zelenka2022] C. Zelenka, M. Kamp, K. Strohm, A. Kadoura, J. Johny, R. Koch, L. Kienle, Automated Classification of Nanoparticles with Various Ultrastructures and Sizes, arXiv preprint (2022) arXiv: 2207.14023.

[Zlotea2014] C. Zlotea, F. Morfin, T. S. Nguyen, N. T. Nguyen, J. Nelayah, C. Ricolleau, M. Latroche, L. Piccolo, Nanoalloying bulk-immiscible iridium and palladium inhibits hydride formation and promotes catalytic performances, Nanoscale 6 (2014) 9955–9959.

CAPTIONS

Fig. 1. a) to d): TEM images of commonly-observed nanostructures of AuFe NPs, together with their schematic representations depicted underneath where gold atoms are represented in gold and iron atoms in grey. a) core-shell (CS) NPs with iron core and gold shell, b) and c) nested core-shell (NCS) NPs, with one or many cores and d) alloy NPs with disordered solid solution mixture. e) and f) nanostructures formed upon *in situ* heating from CS NPs.

Fig. 2. a) Architecture of the deposited AuFe thin film (HAADF STEM micrograph of the cross-section slice of the film produced by focused-ion beam). The $Au_{56}Fe_{44}$ layer coated by a 10-nm thick gold layer to protect iron from air oxidation. b) to e) Elemental EDX maps of Au, Fe, Si and O showing the distribution of elements within the film. f) TEM bright field image of the film showing its columnar structure.

Fig. 3. Overview of nanoparticles produced by nanosecond-pulsed discharges in liquid nitrogen. High-angle annular dark field image of a set of nanoparticles. STEM-EDX elemental maps of Au (from M_α transition), Fe (K_α), W (L_α), Si (K_α) and O (K_α). In this example, nanoparticles are weakly oxidized and made of Au, Fe and traces of W and Si. Localized EDX measurements performed on 5 different spots are materialized by crosses in the HAADF image. Corresponding compositions are given in the table in at.%. We recall here that the nominal composition of the PVD thin film is 56%Au-44%Fe.

Fig. 4. Examples of the three types of small AuFe nanoparticles synthesised by nanosecond-pulsed discharges in liquid nitrogen with similar sizes and Fe/Au ratios: core-shell, segregated and homogeneous. High-angle annular dark-field images. STEM-EDX elemental maps of gold (from M_α transition) and iron (K_α) and their distribution profiles along the red dotted lines. Average compositions (with and without oxygen) are given for each particle in the table. They are determined from areas showed by dotted circles in HAADF images.

Fig. 5. a) Fast-Fourier transform (top) of the yellow-framed area in the TEM-image shown in b) and diffraction pattern (bottom) made of the same region. 3 spots were selected in the FFT image to determine the d-values given in the insert b) Example of slightly-oxidized AuFe nanoparticles with twin defects c) Another example of AuFe nanoparticles with d-spacing showed in e) and f) that matches with the $Fe_{40}Au_{60}$ structure identified in the PVD film d) Example of a highly faulted AuFe nanoparticles with twin defects e) and f) High-resolution images of the areas in dotted frames showing the well-crystallized structure of the nanoparticles and the surface oxide layer. g) Au-Fe phase diagram locating the composition of the AuFe homogeneous nanoparticles and the composition of the PVD thin film. h) Estimates of the iron concentration in the iron content in the AuFe homogeneous nanoparticle from Vegard's law.

Fig. 6. Overview of particles produced by nanosecond-pulsed discharges in liquid nitrogen. Bright field STEM image. TEM-EDX elemental maps of Au (from M_α transition), Fe (K_α), W (L_α), Si (K_α) and O (K_α). In this example, the largest (submicrometric, *i.e.* > 100 nm in diameter) particles (depicted by arrows) are Si@AuFe, Si, Si@Fe and W (**Fig. S4**, **Supplementary Material**).

Fig. 7. *In situ* heat treatment of a Si@AuFe particle, weakly oxidized (Si: 79, Fe: 10, Au: 10, O: 0.5, W: 0.5 at.%). Top: HAADF STEM images of the particle. Middle and bottom: HAADF STEM image and elemental maps of the nanoparticles before and after heating. Arrows in HAADF image (bottom line) indicate two areas uncovered by Au and W and revealing the silicon core. Gold and iron islands forming separate networks, present before heating, coarsen and form larger separate domains. Average compositions of particles are given before and after heating.

Fig. 8. Examples of two Si@AuFe particles (bright field STEM images, top – 225 nm in diameter ; before heating Si: 63, Fe: 21, Au: 15, O: 0.5, W: 0.5 at.% – and middle – 160 nm ; before heating Si: 56, Fe: 25, Au: 13.5, O: 0.5, W: 5 at.% –) heated from room temperature to 1173 K (900°C). Bottom: three silicon particles (145, 150 and 180 nm in diameter ; after heating Si: 95.5, Fe: 0.5, Au: 1, O: 2.5, W: 0.5 at.%), submitted to the same heat treatment. The Au, Fe and Si elemental maps are also provided for the initial and final states. A schematic of the final shape of the two Si@AuFe particles at 900°C is added on the left-hand side of the right column. For the middle one, at 1073, the SiFe core facetted by gold pyramids is clearly visible. Silicon distribution in the AuFe particle at the top overlaps those of Au and Fe. Average compositions are given before and after heating. Complementary information is given in **Fig. S7**, **Supplementary Material**.

Fig. 9. Possible mechanisms for the formation of AuFe NPs and Si@AuFe large particles. a) If the PVD coating is not fully etched, AuFe NPs are synthesized and adopt different structures in the discharge: homogeneous, nested core-shell or core-shell from short to long residence time. b) If the PVD coating is fully etched, large particles made of silicon and containing variable amounts of gold and iron are ejected from the impact area.

Mixing Gold and Iron in nanoparticles by electrical discharges in liquid: a new approach

A.V. Nominé[1], T. Gries[1], C. Noel[1], J. Ghanbaja[1], S. Bruyère[1], A. Nominé[1,2], V. Milichko[1,2], T. Belmonte[1,*]

1. Université de Lorraine, CNRS, IJL, F-54000 Nancy, France
2. ITMO University, St. Petersburg 197101, Russia

* thierry.belmonte@univ-lorraine.fr

SUPPLEMENTAL MATERIAL 1

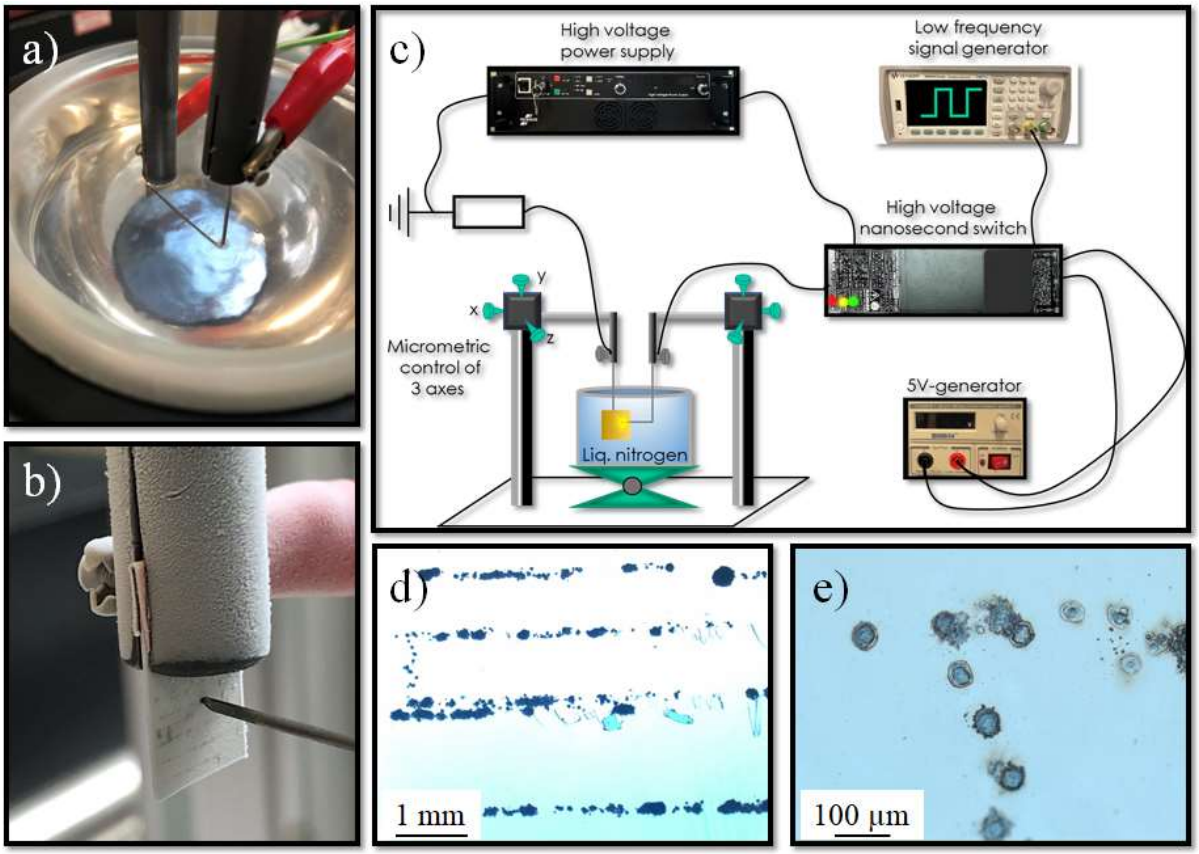

Fig. S1. a) Picture of the Dewar vessel with a silicon wafer placed on the bottom to collect the produced nanoparticles. The anode (with the shape of an L) on the right faces the grounded plate electrode. b) Picture of the 1x1 cm^2 plate electrode (silicon wafer coating by the AuFe thin film), taken out of liquid nitrogen, just after treatment. c) Schematic of the experimental setup. d) set of impacts created on the plate electrode after the scan of the pin electrode and the creation of successive discharges. e) example of single impacts in a row**.**

SUPPLEMENTAL MATERIAL 2

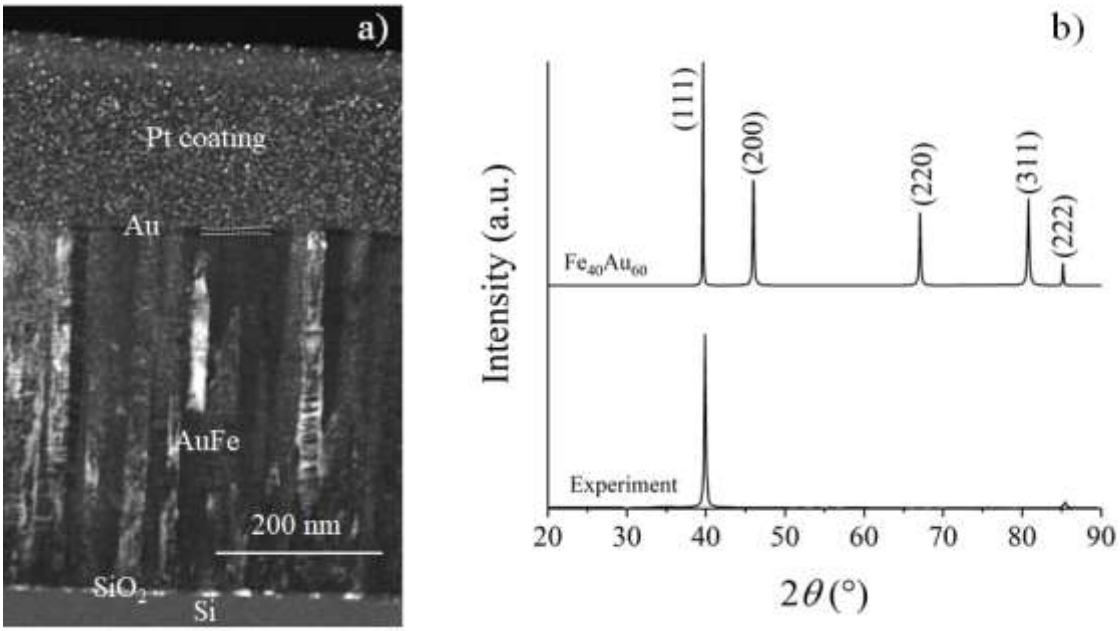

Fig. S2. a) Dark-field TEM image of the cross section of a focused-ion beam slice of the PVD thin film deposited on silicon. The SiO_2 layer at the bottom interface and the Au layer on top are clearly visible. Columns are also easy to distinguish. Platinum is due to the preparation method of the slice by focused-ion beam. b) XRD pattern comparing the experimental recorded spectrum and the reference spectrum corresponding to $Fe_{40}Au_{60}$ The strong texturation of the sample is clear. The thickness of this sample is about 440 nm (slightly thinner that those reported in the main text).

SUPPLEMENTAL MATERIAL 3

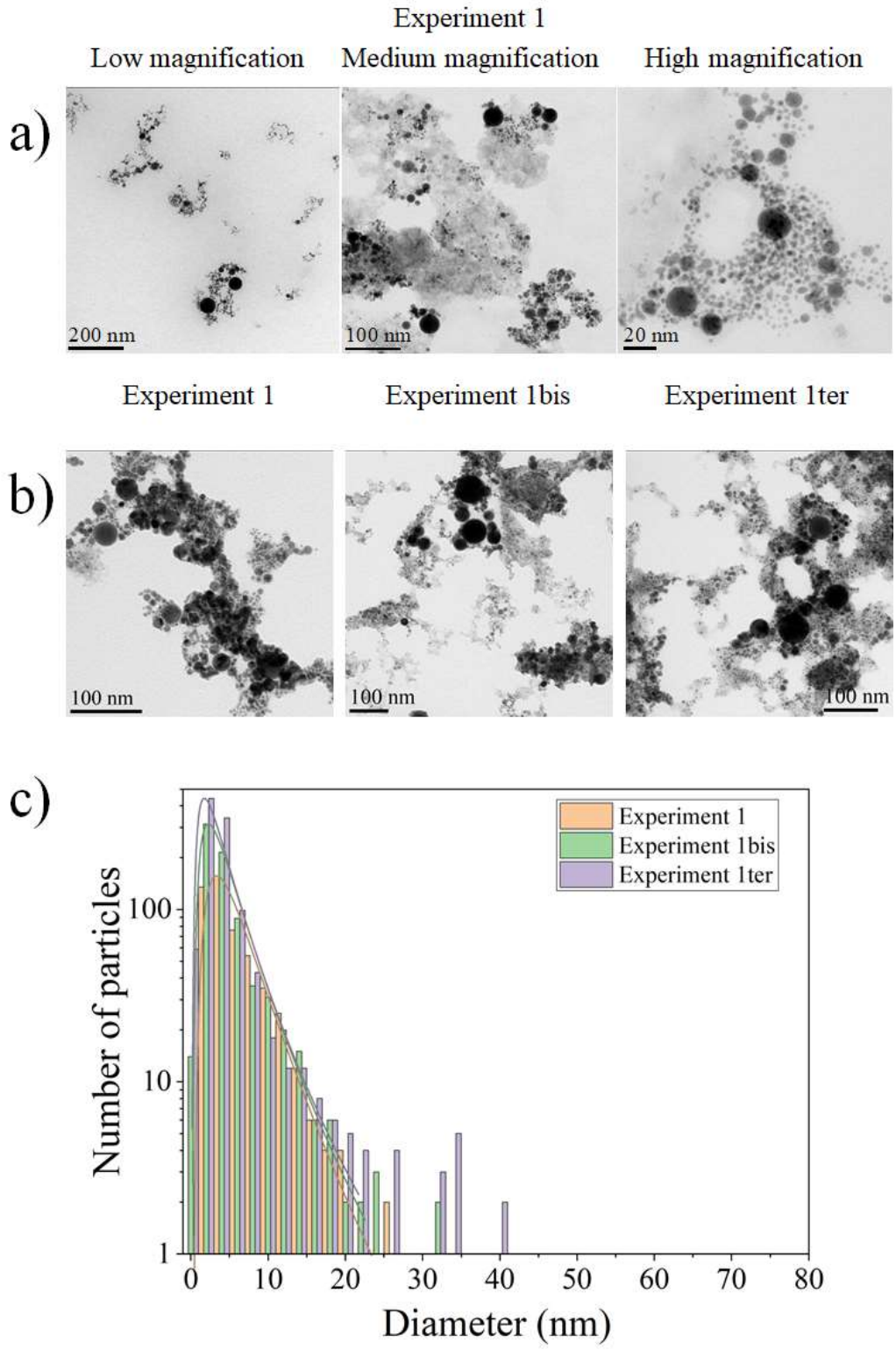

Fig. S3. a) Overview images given at three different magnifications of nanoparticles produced in experiment 1. b) Replicas of experiment 1 used to check the reproducibility of size distributions. c) Distributions of diameters (bars and corresponding lognormal curves) of small and intermediate nanoparticles measured from images given in b). Submicrometric particles ranging from 100 to 500 nm typically have an occurrence of several units.

SUPPLEMENTAL MATERIAL 4

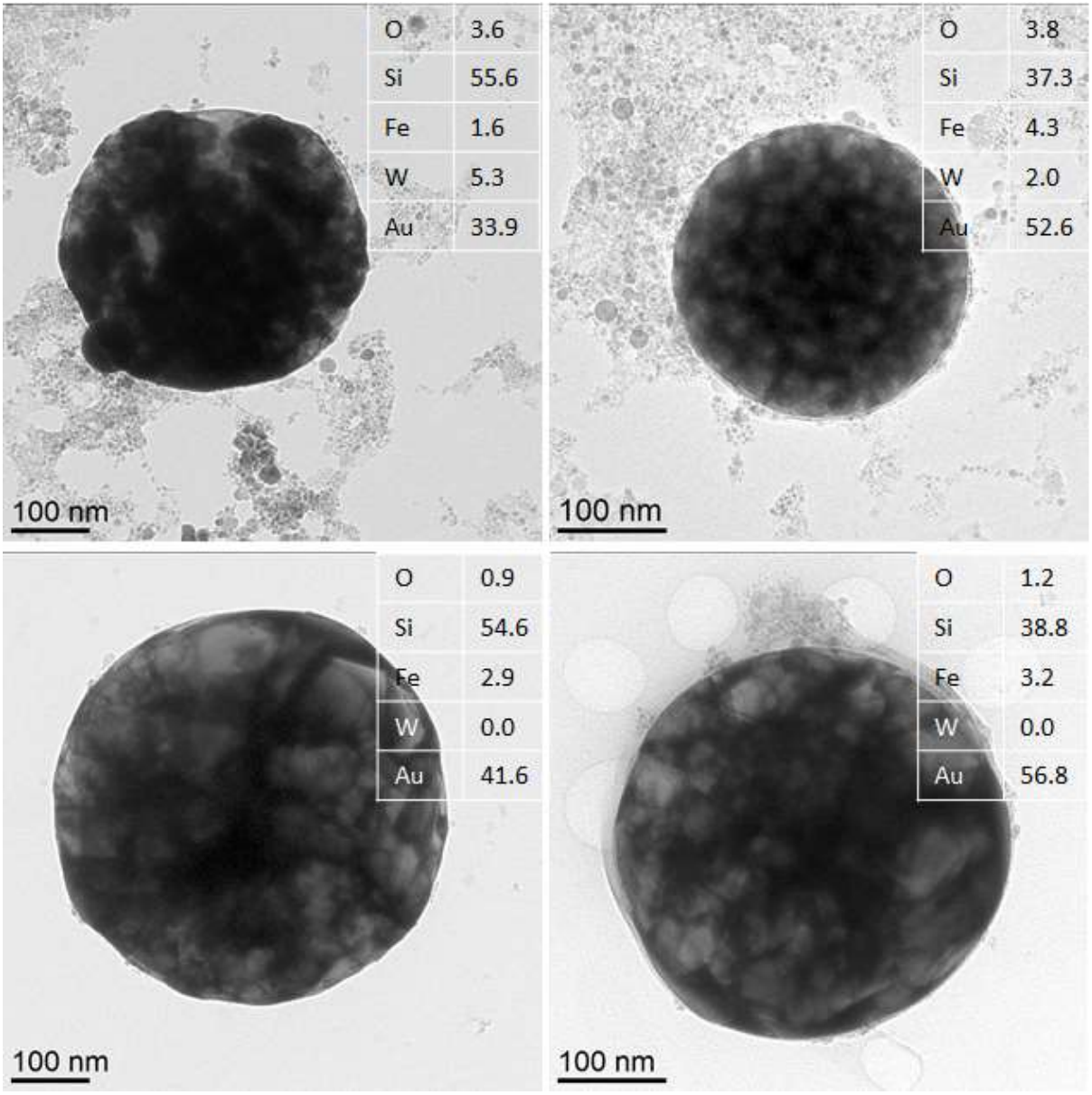

Fig. S4. BF TEM images of Si@Au submicrometric particles, Fe and W are present as trace elements. The particles are metallic, with a weak oxygen content corresponding to a surface oxidation.

SUPPLEMENTAL MATERIAL 5

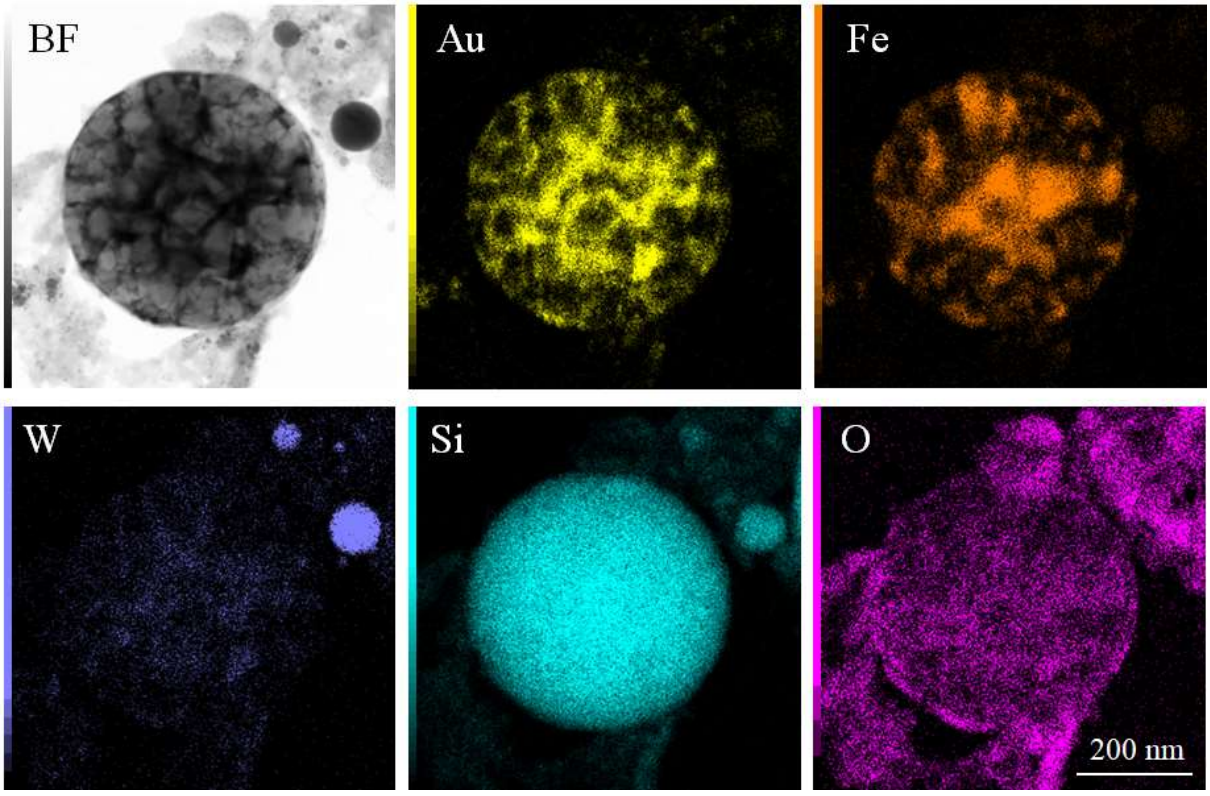

Fig. S5. Example of a large Si@AuFe particle made of Si (core) coated by Fe, Au and traces of W (Si: 78.5, Fe: 12, Au: 9, O = 0.3, W = 0.2 at.%). The particle is hardly oxidized, the oxygen map overlapping pretty well the iron map. BF TEM image shows the presence of a surface pattern where Au and Fe do not mix. STEM-EDX elemental maps are given for Au, Fe, W, Si and O.

SUPPLEMENTAL MATERIAL 6

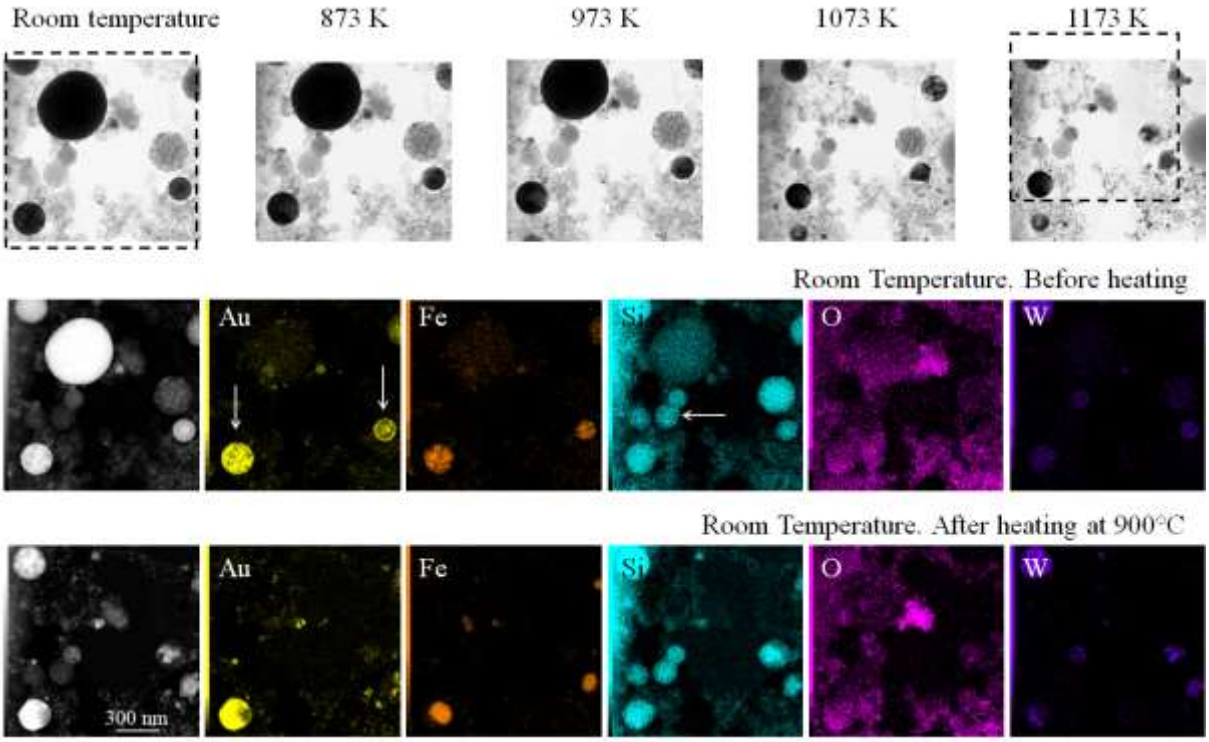

Fig. S6. *In situ* heat treatment of particles, with a special attention paid to two Si@AuFe (vertical arrows) and three Si (horizontal arrow) specimens Top: TEM bright-field images of particles. Frames denote the position of elemental maps showed underneath. Middle and bottom: HAADF image and elemental maps of the nanoparticles before and after heating.

SUPPLEMENTAL MATERIAL 7

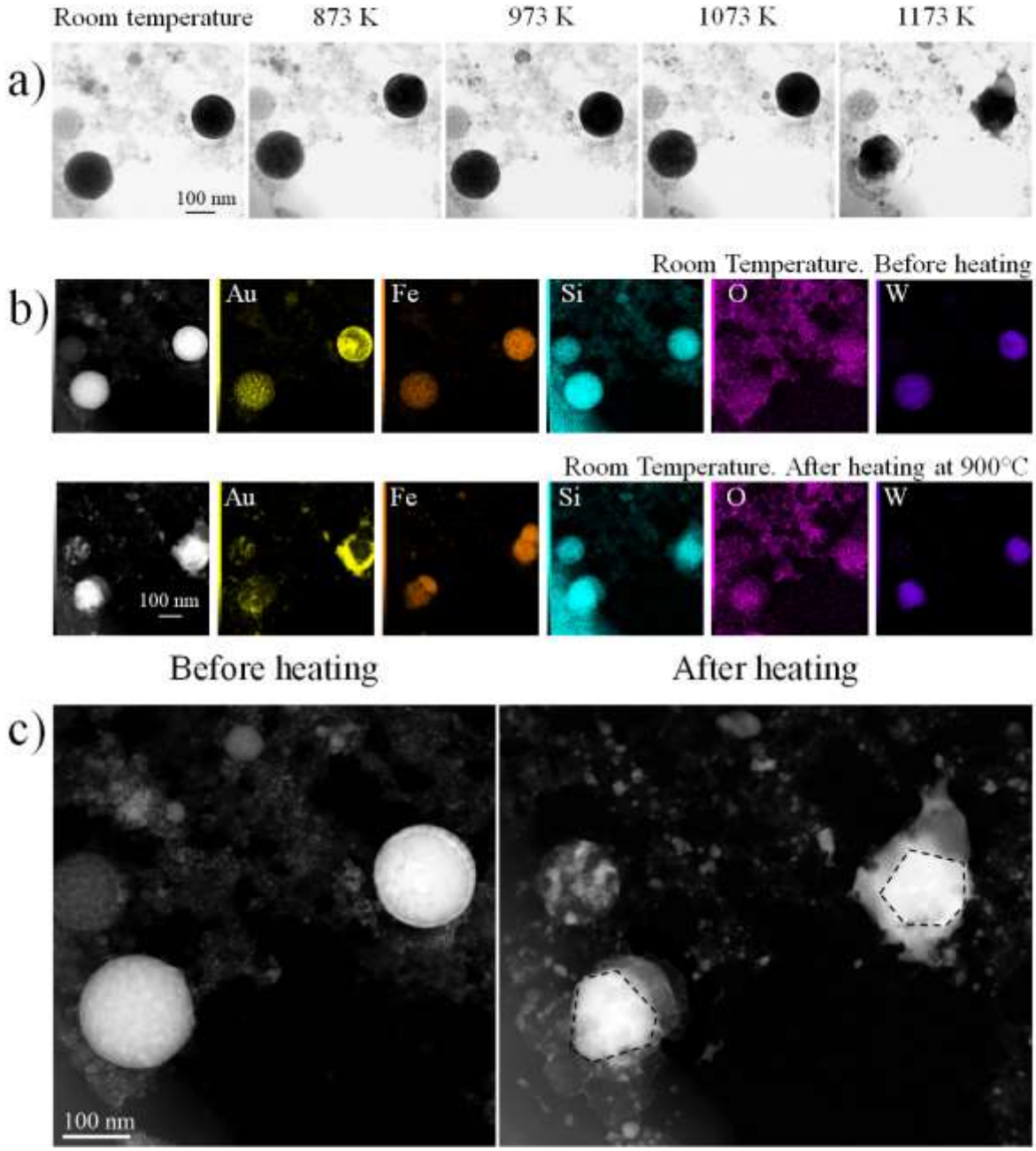

Fig. S7. *In situ* heat treatment of two large Si@AuFe particles. a) Bright-field TEM images of particles. b) HAADF STEM image and elemental maps of the particles before and after heating. c) magnification of particles in b) showing the presence of facetted particles after heating. This second example shows, like **Fig. 7**, the formation of a particle with a AuFe Janus shell (left hand side - before heating: Si: 73.5, Fe: 12.5, Au: 10.5, O: 0.5, W: 3 at.%) and the formation of segregated particle (right hand side - before heating: Si: 56, Fe: 24.5, Au: 13.5, O: 0.5, W: 5 at.%).

SUPPLEMENTAL MATERIAL 8

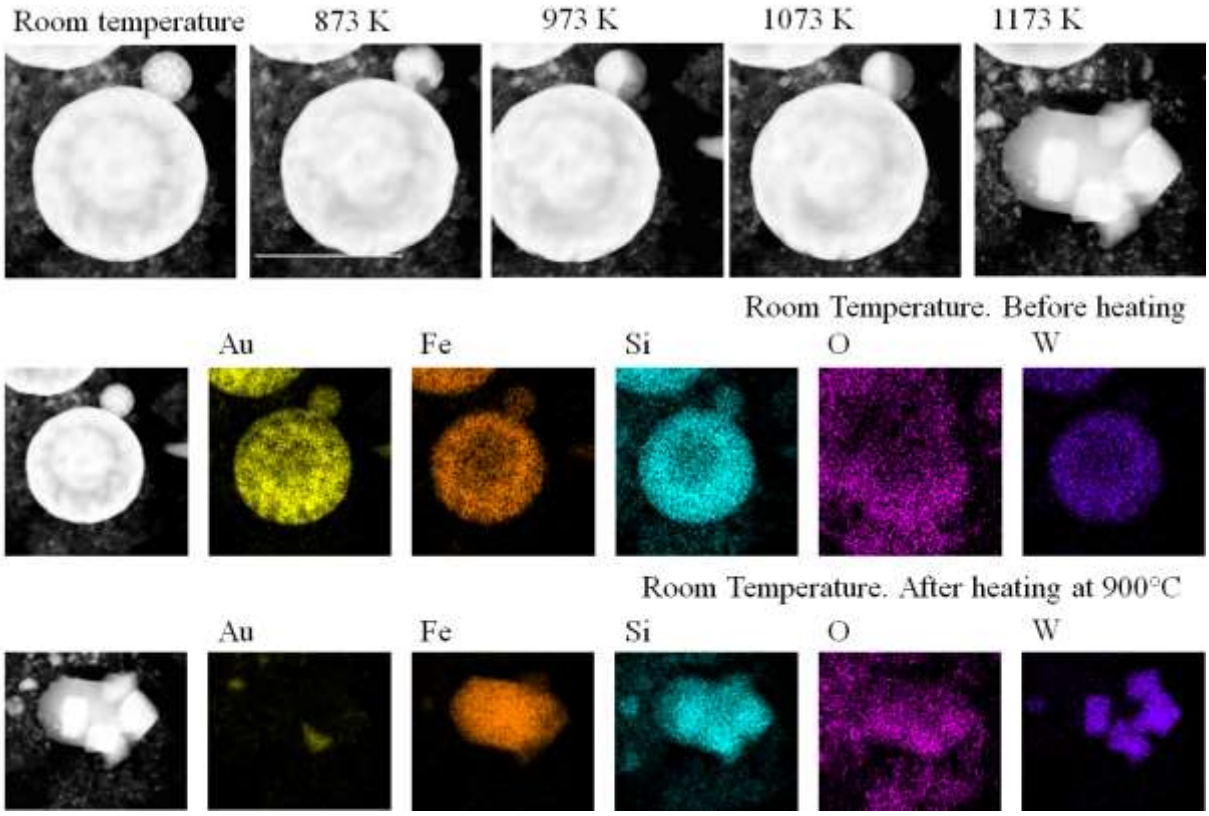

Fig. S8. *In situ* heat treatment of two large Si@AuFe particles. Top: HAADF STEM images of particles. Middle and bottom: HAADF STEM image and elemental maps of the particles before and after heating. This example illustrates, like **Fig. 7**, the evolution of the morphology of spherical objects into SiFe and SiW facetted particles.